nanomaterials

MDPI

Article

Graphene Bridge for Photocatalytic Hydrogen Evolution with Gold Nanocluster Co-Catalysts

Hanieh Mousavi [1], Thomas D. Small [1], Shailendra K. Sharma [2], Vladimir B. Golovko [2], Cameron J. Shearer [1,*] and Gregory F. Metha [1,*]

[1] Department of Chemistry, University of Adelaide, Adelaide, SA 5005, Australia
[2] The MacDiarmid Institute for Advanced Materials and Nanotechnology, School of Physical and Chemical Sciences, University of Canterbury, Christchurch 8140, New Zealand
* Correspondence: cameron.shearer@adelaide.edu.au (C.J.S.); greg.metha@adelaide.edu.au (G.F.M.)

Abstract: Herein, the UV light photocatalytic activity of an Au_{101}NC-$AlSrTiO_3$-rGO nanocomposite comprising 1 wt% rGO, 0.05 wt% $Au_{101}(PPh_3)_{21}Cl_5$ (Au_{101}NC), and $AlSrTiO_3$ evaluated for H_2 production. The synthesis of Au_{101}NC-$AlSrTiO_3$-rGO nanocomposite followed two distinct routes: (1) Au_{101}NC was first mixed with $AlSrTiO_3$ followed by the addition of rGO (Au_{101}NC-$AlSrTiO_3$:rGO) and (2) Au_{101}NC was first mixed with rGO followed by the addition of $AlSrTiO_3$ (Au_{101}NC-rGO:$AlSrTiO_3$). Both prepared samples were annealed in air at 210 °C for 15 min. Inductively coupled plasma mass spectrometry and high-resolution scanning transmission electron microscopy showed that the Au_{101}NC adhered almost exclusively to the rGO in the nanocomposite and maintained a size less than 2 nm. Under UV light irradiation, the Au_{101}NC-$AlSrTiO_3$:rGO nanocomposite produced H_2 at a rate 12 times greater than Au_{101}NC-$AlSrTiO_3$ and 64 times greater than $AlSrTiO_3$. The enhanced photocatalytic activity is attributed to the small particle size and high loading of Au_{101}NC, which is achieved by non-covalent binding to rGO. These results show that significant improvements can be made to $AlSrTiO_3$-based photocatalysts that use cluster co-catalysts by the addition of rGO as an electron mediator to achieve high cluster loading and limited agglomeration of the clusters.

Keywords: gold nanocluster; reduced graphene oxide; $SrTiO_3$; photocatalysis; hydrogen evolution reaction

Citation: Mousavi, H.; Small, T.D.; Sharma, S.K.; Golovko, V.B.; Shearer, C.J.; Metha, G.F. Graphene Bridge for Photocatalytic Hydrogen Evolution with Gold Nanocluster Co-Catalysts. *Nanomaterials* **2022**, *12*, 3638. https://doi.org/10.3390/nano12203638

Academic Editor: José M. Doña-Rodríguez

Received: 19 September 2022
Accepted: 10 October 2022
Published: 17 October 2022

1. Introduction

Green Hydrogen (H_2) is an alternative clean and renewable energy source for the global transition toward net-zero carbon emissions [1]. Currently, over 95% of H_2 is produced from fossil-fuel feedstocks which is a major contributor to carbon dioxide (CO_2) emissions [2]. To comply with net-zero carbon emissions guidelines, a complete transition is required for the production, transportation, and consumption of energy. Therefore, H_2 must be generated from renewable sources such as water and energy created from wind, solar, geothermal, tidal, or biomass reforming [3].

Photocatalytic water splitting is one of the most promising approaches for renewable H_2 production. The basis of a photocatalyst is a light absorbing semiconductor (i.e., $SrTiO_3$, TiO_2, etc.) and co-catalysts (commonly metal nanoparticles) [4,5]. After absorbing light with energy equal or greater than its band gap (E_g), a photoexcited electron and a hole are generated in its conduction band (CB) and valance band (VB), respectively [6]. The photoexcited electron can drive reduction reactions, such as hydrogen evolution reaction (HER), while the hole can drive oxidation reactions, such as oxygen evolution reaction (OER). The co-catalyst can increase charge transfer and minimize electron–hole recombination, maximise reactant molecule activation, reaction selectivity, and catalyst stability [7].

The perovskite oxide $SrTiO_3$ has been extensively used since 1980 for H_2 production under UV irradiation due to its outstanding properties [8]. The conduction band minimum (CBM) potential and valence band maximum (VBM) potential make it suitable for H_2/O_2 evolution [9]. Doping of Al^{3+} as low-valence cations into the Ti^{4+} sites ($AlSrTiO_3$) enhances the photocatalytic H_2 production up to an apparent quantum yield (AQY) of 96% at 365 nm, which is the highest reported value for metal oxide photocatalysts [10–12].

Recently, photocatalytic systems incorporating sub-2 nm sized gold nanoclusters (AuNCs) with a specific number of Au atoms stabilized by ligands have triggered great research interest [13–17]. Typically, AuNCs exhibit non-metallic behaviour (HOMO–LUMO gap), as opposed to localized surface plasmon resonance (LSPR) of nanoparticles (i.e., >2 nm). The presence of HOMO–LUMO gaps in ultra-small AuNCs make them similar to narrow bandgap semiconductors which may be beneficial for photocatalysis [18,19]. AuNCs as co-catalysts can be coupled with semiconductors, resulting in charge transfer which prevents electron–hole recombination [20–22]. The catalytic activity of AuNCs is dependent on a number of factors, such as cluster size/structure, ligand type, ligand density, type of support, and metal–support interaction [23]. Use of triphenylphosphine (PPh_3) ligands provides a simple approach to synthesize AuNCs with small cluster size, narrow size distribution, and easy ligand derivatization. These features make PPh_3-ligated AuNCs unique and different from AuNCs protected by other ligands [23]. As a result, PPh_3-ligated AuNCs as the key components of functional materials offer opportunities for both fundamental studies and potential applications, including photocatalysis [16,18,24–26].

PPh_3-ligated AuNCs do not adhere strongly to metal oxide surfaces. Metal oxides have been shown to fragment PPh_3-ligated AuNCs [27]. It has been reported that the deposition of $Au_n(PPh_3)_m$ (n: 1, 8, 9, 101) on acidic supports occurs according to two pathways, where the cluster–support interaction is affected by Brønsted and/or Lewis acid sites on the support. The interaction of PPh_3 ligands with Brønsted acid on the supports results in cluster break down by "oxidative fragmentation" [27]. Lewis acid sites on the support results in ligand migration from the Au clusters to the support without fragmentation of the clusters, and their subsequent agglomeration [27].

We have previously reported that the uniform loading of Au_{101}NCs onto reduced graphene oxide (rGO) with no aggregation is facilitated via non-covalent interactions through π–π stacking between the phenyl groups of PPh_3 and rGO [28]. rGO with sp^2-hybridized 2D structure has extraordinary properties, such as high electrical conductivity, large surface area, charge mobility, and chemical stability [29]. Due to its large surface area, rGO can serve as an "encapsulant" and wrap around semiconductor nanoparticles [30]. Furthermore, rGO as an electron acceptor/mediator facilitates transfer of photo-generated electrons through its π network to the active sites caused by high charge mobility and conductivity, which inhibits electron–hole recombination and promotes photocatalytic H_2 production [31]. In addition, the tendency of AuNCs to aggregate (either during deposition or activation on the support [32,33]), or deactivate (following initial reaction [34] or under light illumination [20]) is inhibited due to the strong metal support interaction between rGO and AuNCs [28]. The aforementioned features make rGO a desirable candidate to integrate with a broad range of nanomaterials to form nanocomposites with improved performances in photocatalysis.

Herein, we compare two methods to synthesize a photocatalyst incorporating $Au_{101}(PPh_3)_{21}Cl_5$ co-catalyst, rGO electron mediator, and $AlSrTiO_3$ semiconductor. The photocatalytic activity of these nanocomposites was evaluated in photocatalytic HER. Our results highlight the importance of rGO in the synthesis of the nanocomposite to both reduce agglomeration and act as an electron mediator.

2. Materials and Methods

2.1. Reagents and Materials

All chemicals were used as received throughout the study, unless otherwise stated: Natural graphite flakes (Uley, Eyre Peninsula, South Australia), 98% sulfuric acid (H_2SO_4,

RCI Labscan), 85% phosphoric acid (H_3PO_4, Chem-Supply), 70% nitric acid (HNO_3, Chem-Supply), 32% hydrochloric acid (HCl, RCI Labscan), 30% hydrogen peroxide (H_2O_2, Chem-Supply), potassium permanganate ($KMnO_4$, Merck), $Au_{101}(PPh_3)_{21}Cl_5$ was synthesized following the method described by Hutchison and co-workers [35], $AlSrTiO_3$ was provided by K. Domen (University of Tokyo and Shinshu University) and was synthesized following the method described by Ham et al. [10], methanol (CH_3OH, Merk, Analysis Grade), high-purity Milli-Q water (18.2 MΩ cm at 25 °C), gold single component standard ICP (TraceCERT, Merck, 999 mg L^{-1}), 68 Component ICP-MS Standard (High Purity Standards, HPS, 10 µg mL^{-1}).

2.2. *Au_{101}NC-$AlSrTiO_3$-rGO Photocatalyst Preparation*

The procedure for fabrication of $AlSrTiO_3$ with controlled content of 1 wt% rGO and 0.05 wt% Au via an ex situ method is schematically presented in Figure 1.

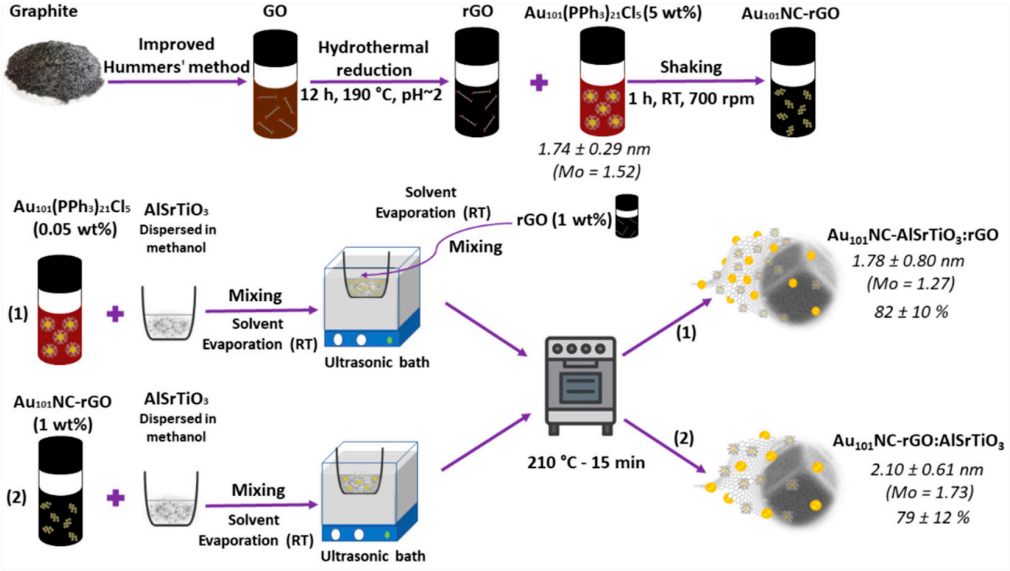

Figure 1. Schematic illustration of synthesis of Au_{101}NC-rGO nanocomposite and (1) Au_{101}NC-$AlSrTiO_3$:rGO and (2) Au_{101}NC-rGO:$AlSrTiO_3$ with 1 wt% rGO and 0.05 wt% Au. The values on the right-hand side show the Au cluster diameter measured by TEM and final gold loading measured by ICP-MS.

2.2.1. Graphene Oxide, rGO, and Au_{101}NC-rGO Synthesis

Graphene oxide (GO), rGO, and Au_{101}NC-rGO nanocomposite were synthesized following our previously reported method [28]. In brief, GO was synthesized via the improved Hummers' method and then was reduced by hydrothermal treatment at 190 °C for 12 h in a 500 mL Teflon-lined stainless-steel autoclave. To obtain the 5 mg Au_{101}NC-rGO nanocomposite with 5 wt% Au loading in 1.5 mL methanol, the as-obtained Au_{101}NC was dispersed in methanol (1 mg mL^{-1}). Then, 320 µL Au_{101}NC dispersion (corresponding to 0.25 mg non-ligated Au mass) was added dropwise to 830 µL magnetically stirred as-synthesized rGO dispersion in methanol (5.70 mg mL^{-1}) under ambient temperature and made up to 1.5 mL with methanol. The mixture was wrapped immediately with aluminium foil followed by mixing using an incubator and orbital shaker (THERMOstar), for 1 h at room temperature (RT) and 700 rpm.

2.2.2. Au_{101}NC-$AlSrTiO_3$-rGO Synthesis

The synthesis of Au_{101}NC-$AlSrTiO_3$-rGO with 1 wt% rGO and 0.05 wt% Au (corresponding to 0.0025 mg non-ligated Au mass) was carried out via two different routes, each with 2 steps, as shown in Figure 1 (Hyphen (-) is used to show the two components are first mixed and colon (:) is used to show the component is added last):

(1) Au_{101}NC-$AlSrTiO_3$:rGO: To obtain 25 mg Au_{101}NC-$AlSrTiO_3$:rGO, 16.0 µL Au_{101}NC dispersion (1 mg mL^{-1} ligated Au mass) was added dropwise to 25 mg of $AlSrTiO_3$ dispersed in 5 mL methanol in a porcelain evaporation dish and homogenized using bath sonication at RT until the solvent was completely evaporated. The as-obtained Au_{101}NC-$AlSrTiO_3$ was dispersed and homogenized in 5 mL methanol via sonication (2 min). Then, 41.7 µL as-synthesized rGO dispersion (5.70 mg mL^{-1}) was added dropwise to the dispersion with bath sonication at RT until the solvent was completely evaporated. The as-obtained Au_{101}NC-$AlSrTiO_3$:rGO was annealed in air in a muffle furnace (S.E.M Pty. Ltd., Adelaide, Australia) at 210 °C for 15 min.

(2) Au_{101}NC-rGO:$AlSrTiO_3$: To obtain 25 mg Au_{101}NC-rGO:$AlSrTiO_3$, 0.25 mg (75 µL) of the as-synthesized Au_{101}NC-rGO nanocomposite was added dropwise to 25 mg of $AlSrTiO_3$ dispersed in 5 mL methanol in a porcelain evaporation dish. The dispersion was homogenized using bath sonication at RT until the solvent had evaporated. The as-obtained Au_{101}NC-rGO: $AlSrTiO_3$ was annealed in air in a muffle furnace at 210 °C for 15 min.

2.3. Characterization

Characterization of obtained materials before and after photocatalysis was performed using: scanning electron microscopy (SEM), high-angle annular diffraction field scanning transmission electron microscopy (HAADF-STEM), bright filed scanning transmission electron microscopy (BF-STEM), inductively coupled plasma mass spectrometry (ICP-MS), and UV–visible diffuse reflectance spectroscopy (UV–Vis DRS).

2.3.1. UV–Visible Diffuse Reflectance Spectroscopy (UV–Vis DRS)

UV–Vis DRS measurements were used to infer the extent of Au_{101}NC agglomeration and to confirm that co-catalysts (rGO and Au_{101}NC) did not affect the bandgap of the photocatalyst ($AlSrTiO_3$). UV–Vis DRS measurements were obtained using a spectrophotometer (Cary 5000 UV–Vis–NIR) fitted with a Praying Mantis Diffuse Reflection accessory (Harrick, DRP-SAP). A PTFE disc was used as reflectance standard. For each measurement, the sample holder was filled with approximately 15 mg of the solid-state sample and the reflectance was measured from 200–800 nm.

2.3.2. Scanning Electron Microscopy (SEM)

The surface morphology, agglomeration state of Au_{101}NC, and interaction of rGO sheets with $AlSrTiO_3$ were measured using a High-Resolution Field Emission Scanning Electron Microscope equipped with EDX Silicon Drift Detectors (FEI-SEM Quanta 450).

2.3.3. High-Angle Annular Dark-Field Scanning TEM (HAADF-STEM)

Images showing the effect of heating and UV irradiation on the size and distribution of Au_{101}NC over $AlSrTiO_3$ and rGO along with interaction of Au_{101}NC, rGO, and $AlSrTiO_3$ with each other were acquired with a FEI Titan Themis STEM operating at 200 keV. The STEM was equipped with a Super-X EDS detector in conjunction with a low-background sample holder to minimize Cu background peaks and maximize X-ray collection efficiency. EDS data were analysed using the Velox™ software from Thermo Fisher Scientific. Samples were prepared by dropping prepared dispersions of as-prepared materials (sonicated for 1 min) onto a 300-mesh copper grid with a lacey carbon support film. The solvent was then allowed to evaporate before placing it into the sample holder for analysis. Image J was employed to measure the size of Au particles (200 particles).

2.3.4. Inductively Coupled Plasma Mass Spectrometry (ICP-MS)

ICP-MS (Agilent 8900x QQQ) was employed to determine the total content of Au in Au_{101}NC-rGO, Au_{101}NC-rGO:$AlSrTiO_3$, Au_{101}NC-$AlSrTiO_3$, and Au_{101}NC-$AlSrTiO_3$:rGO by measuring the amount of Au that remained in solution (i.e., not adsorbed onto the solid). The as-synthesized sample dispersions in methanol (1 mL) were centrifuged to precipitate

any solid, followed by filtration of the supernatant liquid using a Whatman 13 mm, 0.1 µm disposable nylon syringe filter. Then, 0.05 mL of filtrate was taken, and the solvent was allowed to evaporate. To dissolve the remaining solid, 0.2 mL of fresh aqua regia (analysis grade reagents of 32% hydrochloric acid and 70% nitric acid) was added and left for 30 min, then filled up to 25 mL with water for analysis. Gold and phosphorous single standard solutions in 2% *aqua regia* with concentrations of 5, 10, 25, 50, 100 and 200 ppb were used for calibration.

2.4. Photocatalysis

Photocatalytic HER was performed in a sealed overhead-irradiation type glass batch reactor (1.7 cm^2). For each photocatalytic reaction, 7 mg of sample was immersed in 3 mL of methanol:H_2O (1:2) and sonicated for 1 min to form a homogeneous suspension. Before each reaction, air was evacuated from the system and replaced with Ar (1 atm). The suspension was then irradiated with a UV LED (365 nm, 83 mW/cm^2, Hongkong UVET Co., UH-82F+L12) for 2 h and stirred during irradiation using a magnetic bar. Starting at 0 h, the evolved gases were sampled hourly and analysed by gas chromatography (Agilent Technologies, 7890B, thermal conductivity detector, Ar carrier gas, molecular sieve 5 Å column).

3. Results and Discussion

The 3 component (Au_{101}NC, $AlSrTiO_3$, and rGO) photocatalysts with 1 wt% rGO and 0.05 wt% Au was prepared by a sequential mixing process via 2 routes. (1) Au_{101}NC was first mixed with $AlSrTiO_3$ followed by the addition of rGO (Au_{101}NC-$AlSrTiO_3$:rGO) and (2) Au_{101}NC was first mixed with rGO followed by the addition of $AlSrTiO_3$ (Au_{101}NC-rGO:$AlSrTiO_3$) (see Figure 1).

Characterization of the Au_{101}NC-$AlSrTiO_3$-rGO nanocomposites was performed to investigate the morphology/structural features, agglomeration state, and interactions between the Au_{101}NCs, $AlSrTiO_3$ and rGO along with their effect on H_2 evolution.

3.1. Physical Characterization of Au_{101}NC-$AlSrTiO_3$-rGO

Figure 2a,b shows the SEM images of Au_{101}NC-$AlSrTiO_3$:rGO and Au_{101}NC-rGO:$AlSrTiO_3$. The SEM images of Au_{101}NC-$AlSrTiO_3$:rGO (Figure 2a) and Au_{101}NC-rGO:$AlSrTiO_3$ (Figure 2b) are similar with no obvious change in the morphology/structure and size relative to $AlSrTiO_3$ (Figure S1). Although the rGO loading on $AlSrTiO_3$ is low (1 wt%) in both nanocomposites, it can be seen in both higher resolution images that the rGO is well dispersed and wraps around some of $AlSrTiO_3$ particles.

Figure 3a–f shows the BF-STEM images and log-normal size-distribution histograms for Au_{101}NC-$AlSrTiO_3$:rGO (Figure 3a–c) and Au_{101}NC-rGO:$AlSrTiO_3$ (Figure 3d–f). Interestingly, compared with the original cluster (mode (Mo) = 1.52 nm, Figure S2) the cluster size decreases for Au_{101}NC-$AlSrTiO_3$:rGO (Mo = 1.27 nm) but increases for Au_{101}NC-rGO:$AlSrTiO_3$ (Mo = 1.73 nm). This suggests the clusters may fragment upon initial interaction with $AlSrTiO_3$. This will be further addressed when discussing the ICP-MS results (*vide infra*).

Beyond determining cluster size, imaging was used to locate where the AuNCs were located, and to determine if this differed for the two synthesis routes (e.g., on rGO or $AlSrTiO_3$). We had expected to observe more Au_{101}NC on the metal oxide in the Au_{101}NC-$AlSrTiO_3$:rGO sample, considering that the first step is the direct mixing of Au_{101}NC with $AlSrTiO_3$ (see Figure S3 for additional images). The STEM images confirm that regardless of the synthetic process, Au_{101}NC was found almost exclusively on the rGO with only very few Au_{101}NC (<5) observed on $AlSrTiO_3$ amongst the thousands of Au_{101}NC observed on rGO within the composite (see Figure S4a for example). This observation shows that the PPh_3 ligated Au_{101}NC has a high tendency to interact with rGO, as found in our previous work [28].

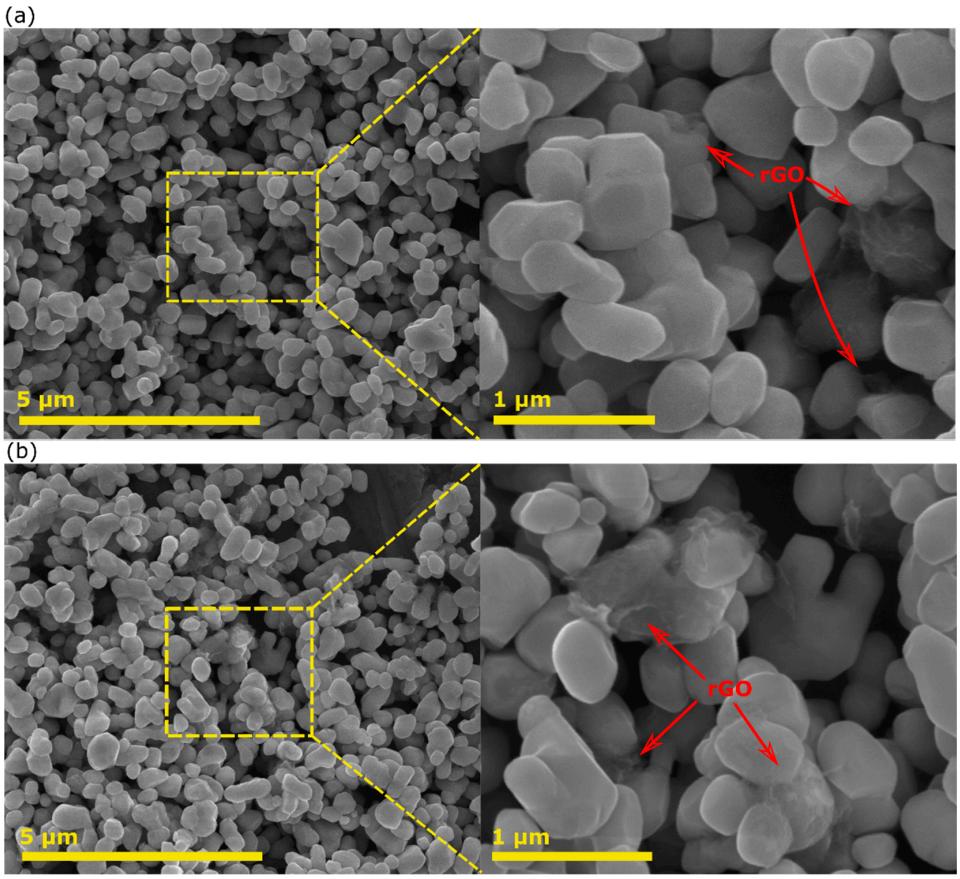

Figure 2. SEM image of (**a**) Au_{101}NC-$AlSrTiO_3$:rGO and (**b**) Au_{101}NC-rGO:$AlSrTiO_3$.

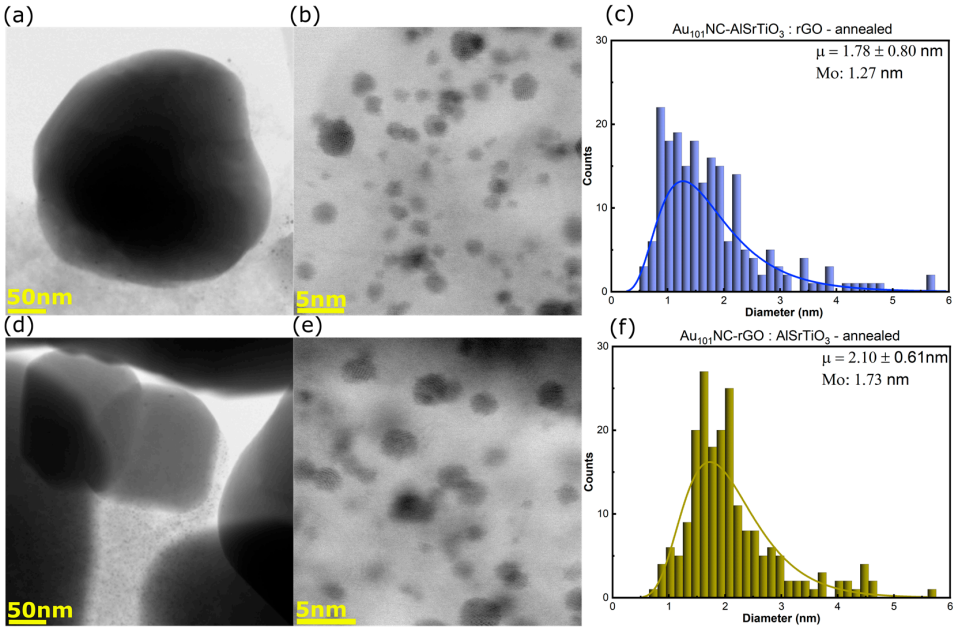

Figure 3. (**a**,**b**) BF-STEM images and (**c**) size distribution histogram of Au_{101}NC-$AlSrTiO_3$:rGO, (**d**,**e**) BF-STEM images and (**f**) size distribution histogram of Au_{101}NC-rGO:$AlSrTiO_3$. Histogram fit to log-normal distribution with labels indicating mean (μ ± standard deviation) and Mo. Annealing was performed in air at 210 °C for 15 min. $AlSrTiO_3$ and Au_{101}NCs are the particles >50 nm and <5 nm, respectively. The grey thin sheets are rGO.

For further investigation, ICP-MS was used to determine the amount of Au deposited onto the rGO or $AlSrTiO_3$ at each step of the synthetic process. This was achieved by measuring the Au that had not adsorbed (i.e., remained in solution after centrifugation). Table 1 shows the values obtained for the Au adsorption and the consequent Au loading at each step.

Table 1. Adsorption (%) of Au on $AlSrTiO_3$ and rGO by ICP-MS.

	Au Adsorption (%)
Au_{101}NC-$AlSrTiO_3$	69 ± 11
Au_{101}NC-$AlSrTiO_3$:rGO	82 ± 10
Au_{101}NC-rGO	95 ± 2
Au_{101}NC-rGO:$AlSrTiO_3$	79 ± 12

When following synthesis route (1); after mixing Au_{101}NC and $AlSrTiO_3$ together we find that 69% of the Au has adsorbed onto the metal oxide surface. In the case when rGO (in methanol) is added to the Au_{101}NC-$AlSrTiO_3$, the adsorption increases to 82%. These adsorptions reflect the higher affinity of Au_{101}NC for rGO. When following the alternate synthesis route (2); we find an initial high adsorption of 95% (Au_{101}NC-rGO) which then decreases to 79% after the addition of $AlSrTiO_3$ in methanol. This is likely due to the dissolution of anchored Au_{101}NC in methanol (Figure S10). The ICPMS results are consistent with the STEM observation that Au_{101}NC are decorating the rGO in the composites with minimal loading on the $AlSrTiO_3$ nanoparticles.

3.2. Photocatalytic Hydrogen Evolution Activity of AuNCs-$AlSrTiO_3$-rGO

Figure 4 presents the effect of co-loading of rGO and Au_{101}NC onto $AlSrTiO_3$ via different routes on photocatalytic HER performance under UV light irradiation for 2 h under sacrificial conditions (methanol as hole scavenger). For comparison, the photocatalytic activity of rGO, $AlSrTiO_3$, Au_{101}NC-rGO, Au_{101}NC-$AlSrTiO_3$, and rGO-$AlSrTiO_3$ as control samples under the same experimental conditions were also evaluated. The trend of H_2 production rate (Table 2) follows: Au_{101}NC-$AlSrTiO_3$:rGO > Au_{101}NC-rGO:$AlSrTiO_3$ > rGO-$AlSrTiO_3$ ~ Au_{101}NC-$AlSrTiO_3$ > $AlSrTiO_3$ > rGO > Au_{101}NC-rGO. The nanocomposite materials Au_{101}NC-$AlSrTiO_3$:rGO and Au_{101}NC-rGO:$AlSrTiO_3$ demonstrate the highest activity, producing 385 ± 22 and 334 ± 24 nmol h^{-1} of H_2, respectively. This is approximately 10 times that of the activity of the rGO-$AlSrTiO_3$ and Au_{101}NC-$AlSrTiO_3$ where $AlSrTiO_3$ was only decorated with either rGO or Au_{101}NCs. Negative control samples rGO, $AlSrTiO_3$, and Au_{101}NC-rGO produced negligible amounts of H_2.

Table 2. Photocatalytic H_2 production rate—with Au mass loading 0.05% (0.0025 mg non-ligated Au): 1:2 methanol:water, 365 nm at 83 mW/cm^2, 2 h reaction time. Error is standard deviation.

Photocatalyst (7 mg)	**H_2 Production Rate (nmol h^{-1})**
rGO	4 ± 0
$AlSrTiO_3$	6 ± 1.4
Au_{101}NC-rGO	3 ± 0
Au_{101}NC-rGO:$AlSrTiO_3$	334 ± 24
Au_{101}NC-$AlSrTiO_3$	33 ± 13
Au_{101}NC-$AlSrTiO_3$:rGO	385 ± 22
rGO-$AlSrTiO_3$	39 ± 9.4

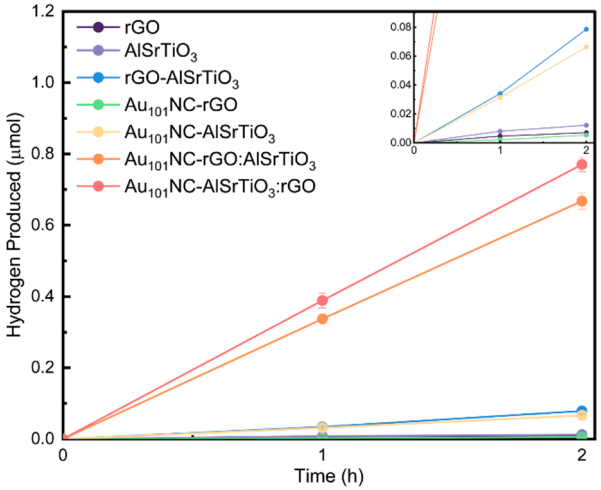

Figure 4. Liquid-phase sacrificial photocatalytic H_2 production of rGO, $AlSrTiO_3$, Au_{101}NC-rGO, Au_{101}NC-$AlSrTiO_3$, rGO-$AlSrTiO_3$, Au_{101}NC-$AlSrTiO_3$:rGO, and Au_{101}NC-rGO:$AlSrTiO_3$. (Conditions: 1:2 methanol:water, LED 365 nm at 83 mW/cm^2 for 2 h). Error bars represent standard error. The inset image is scaled up to display the relative activity of rGO, $AlSrTiO_3$, Au_{101}NC-rGO, and Au_{101}NC-$AlSrTiO_3$.

Extended experiments on the system that we did not completely optimize include the effect of Au_{101}NC loading. Figure S7 indicates that increasing Au mass loading by 20 times (0.05% to 1% wt%) in Au_{101}NC-$AlSrTiO_3$:rGO results in only a small increase in photocatalytic activity (1.6 times). We also altered the annealing condition of the photocatalyst prior to hydrogen evolution. Figure S8 shows that the photocatalytic activity also increases in Au_{101}NC-$AlSrTiO_3$:rGO in order; air annealing > vacuum annealing > not annealed. Further work is required to ascertain the precise reason why annealing in air produced a more active photocatalyst.

STEM was also undertaken after photocatalysis to observe changes in the Au_{101}NC size. Figure 5a–f shows that the average cluster size slightly increased in Au_{101}NC-$AlSrTiO_3$:rGO-HER (Mo from 1.27 to 1.49), and with almost no change for Au_{101}NC-rGO:$AlSrTiO_3$-HER (Mo from 1.73 to 1.72). The changes to the mode reflect changes to the most common cluster size. When comparing the mean average and clusters greater than 2 nm, we see there has been some agglomeration in both samples. The amount of Au particles greater than 2 nm increased from 28.6% to 38.5% (13.5% > 3 nm) and 45.0% to 52.9% (14.8% > 3 nm) for Au_{101}NC-$AlSrTiO_3$:rGO-HER and Au_{101}NC-rGO:$AlSrTiO_3$-HER, respectively (Table 3).

Table 3. A comparison of particle size in Au_{101}NC, Au_{101}NC-$AlSrTiO_3$:rGO, and Au_{101}NC-rGO:$AlSrTiO_3$ before and after HER. Annealing was performed in air at 210 °C for 15 min.

	Mean (nm)	Mode (nm)	>2 nm	>3 nm
Au_{101}NC	1.74 ± 0.29	1.52	25.6%	3.1%
Au_{101}NC-$AlSrTiO_3$:rGO	1.78 ± 0.80	1.27	28.6%	9.9%
Au_{101}NC-$AlSrTiO_3$:rGO-HER	2.06 ± 1.03	1.49	38.5%	13.5%
Au_{101}NC-rGO:$AlSrTiO_3$	2.10 ± 0.61	1.73	45.0%	12.0%
Au_{101}NC-rGO:$AlSrTiO_3$-HER	2.22 ± 0.92	1.72	52.9%	14.8%

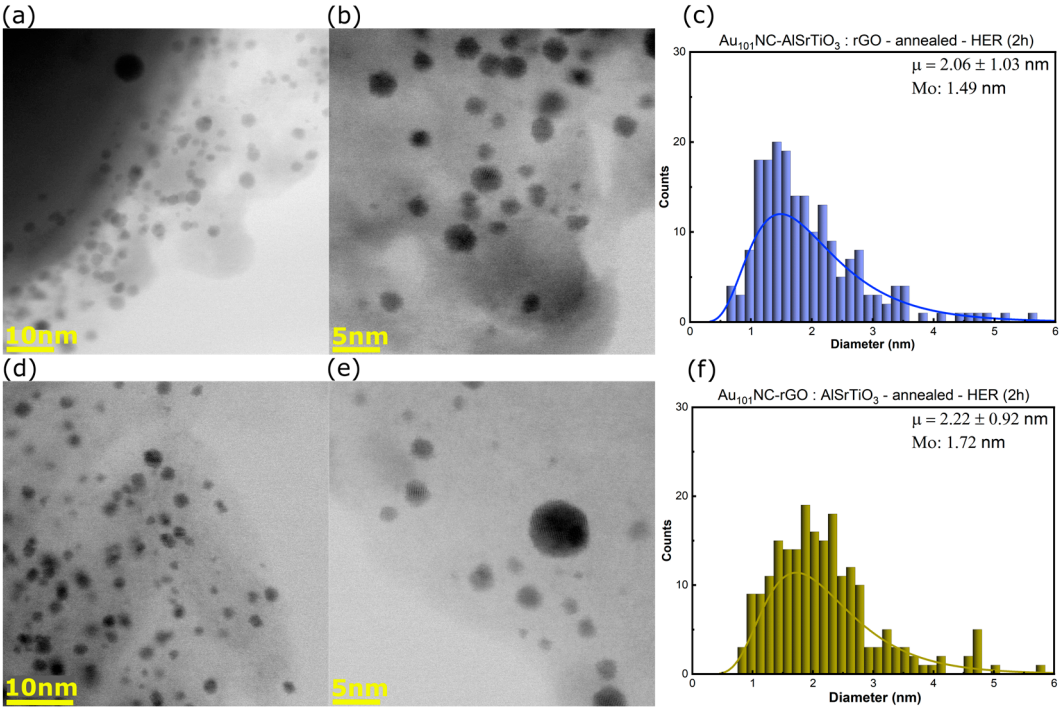

Figure 5. (**a**,**b**) BF-STEM images and (**c**) size distribution histogram of Au_{101}NC-$AlSrTiO_3$:rGO-HER, (**d**,**e**) BF-STEM images and (**f**) size distribution histogram of Au_{101}NC-rGO:$AlSrTiO_3$-HER. Histogram fit to log-normal distribution with labels indicating mean (μ ± standard deviation) and mode (Mo). Annealing was performed in air at 210 °C for 15 min. $AlSrTiO_3$ and Au_{101}NCs are the particles >50 nm and <5 nm, respectively. The grey thin sheets are rGO.

4. Discussion

An efficient photocatalyst must possess three critical properties. A semiconductor with a bandgap able to absorb incident light, an electronic structure able to migrate the photo-generated charges to the particle surface, and the redox potential at the surface-active sites must be suitable for the water splitting reactions. Most photocatalysts, $AlSrTiO_3$ included, can only evolve H_2 with a co-catalyst [36]. This explains the very low H_2 evolved (<7 nmol h^{-1}) in the negative control samples which either do not contain a semiconductor (Au_{101}NC-rGO, rGO) or co-catalyst ($AlSrTiO_3$). When the semiconductor is combined with one of the co-catalyst materials (Au_{101}NC-$AlSrTiO_3$ and rGO-$AlSrTiO_3$) we observe low H_2 evolution (30–40 nmol h^{-1}). rGO itself has been previously shown to have moderate activity as a HER co-catalyst [37]. Our previous work on electrocatalytic HER showed Au_{101}NC was the most active of various gold clusters and far more active than rGO alone [38]. When both rGO and Au_{101}NC are combined with $AlSrTiO_3$, regardless of synthetic route, we observe a significantly enhanced HER activity (330–390 nmol h^{-1}). This is attributed to the contributing role of the rGO to facilitate charge transfer from semiconductor to co-catalyst (Figure 6).

The difference in HER activity of the two synthetic routes that were investigated is small but may be due to the difference in Au_{101}NC after deposition with Au_{101}NC-$AlSrTiO_3$:rGO having a smaller size and slightly greater Au loading. Overall, Au_{101}NC-$AlSrTiO_3$:rGO shows less agglomeration than Au_{101}NC-rGO:$AlSrTiO_3$, the differences in clusters size after HER may also be explained by the difference in cluster size before HER, as observed by STEM (Figure 5 and Table 3). The smaller, fragmented, Au_{101}NC in the Au_{101}NC-$AlSrTiO_3$:rGO sample seem to be more prone to agglomeration under UV irradiation. It is difficult to conclude that the agglomeration is caused by the UV light or charge transfer (photoreduction) from rGO and $AlSrTiO_3$ to Au_{101}NCs. Despite small increases in mean average cluster size, both synthetic routes maintain a mode diameter

of gold as clusters (<2 nm). This is supported by UV–Vis DRS in which the plasmonic band of the AuNCs was not observe in both of Au_{101}NC-$AlSrTiO_3$:rGO and Au_{101}NC-rGO:$AlSrTiO_3$ (Figure S6). This highlights the strong interaction between Au_{101}NCs and rGO prevents cluster agglomeration, which is in agreement with our previous work [28].

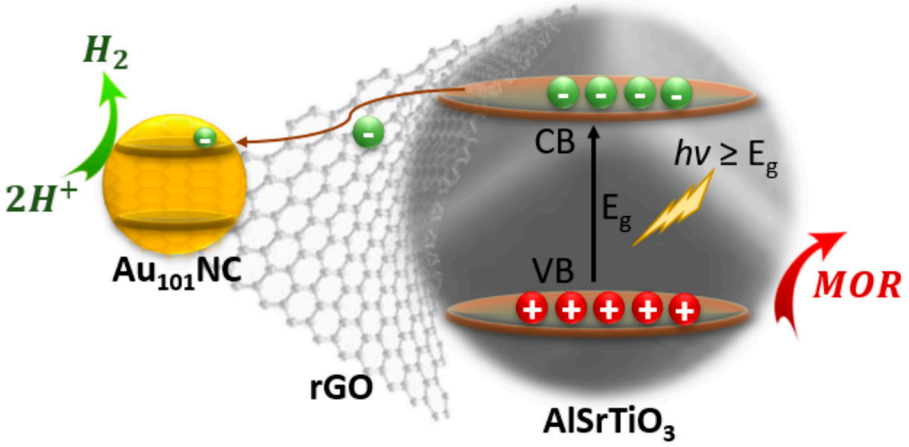

Figure 6. Possible mechanism of electron transfer during photocatalytic H_2 evolution under UV light irradiation. Electrons are transferred from $AlSrTiO_3$ to the CB of Au_{101}NC via rGO. (MOR = methanol oxidation reaction).

These results demonstrate that the properties of the support determine the agglomeration/fragmentation state of Au_{101}NC and the type of interactions between Au_{101}NCs, $AlSrTiO_3$, and rGO which has a large impact on the photocatalytic activity. The introduction of rGO with a large surface area provides more sites for the adsorption of Au_{101}NCs. The synergistic effect between Au_{101}NCs and rGO and higher tendency of Au_{101}NC to interact with rGO results in agglomeration resistance and migration of Au_{101}NC from $AlSrTiO_3$ to rGO. Such selective loading of Au_{101}NCs on rGO over $AlSrTiO_3$ improves the photogenerated exciton separation. The rGO acts as a charge carrier resulting in improved transfer of photo-generated electrons through its π network to Au_{101}NCs as the active site for H_2 production. Our findings suggest that the proposed methodology using Au_{101}NCs with PPh_3 ligands to obtain atom-specific metal clusters can be used in photocatalysis with reduced agglomeration without adding a protecting overlayer (e.g., Cr_2O_3 overlayer for Au_{25} loaded on $BaLa_4Ti_4O_{15}$) [39,40].

The majority of studies on Au co-catalyst systems in photocatalysis focus on nanoparticles where the LSPR is used to extend light absorption into the visible [41,42]. Future work may look at synthesizing size-specific AuNCs which are large enough to exhibit LSPR.

Cluster co-catalysts from metals other than gold have been used in photocatalysis. High density and uniform deposition of Fe, Co, and Ni clusters with sizes less than 1 nm on TiO_2 significantly increased the photocatalytic H_2 evolution activity caused by efficient carrier separation [43]. The photocatalytic H_2 production of Pt_n cluster (n: 8, 22, 34, 46, 68) cluster is affected by the size (number of atoms) of cluster [44]. Therefore, our developed methodology can also be applied with other size-specific PPh_3-ligated metal clusters such as Pt, Pd, Cu, Ni, Co, Ag, and Ir to design highly efficient clusters/rGO nanocomposites for photocatalytic H_2 production.

5. Conclusions

The simple preparation of Au_{101}NC-$AlSrTiO_3$:rGO as a HER photocatalyst is presented for the first time. The incorporation of rGO and Au_{101}NC with $AlSrTiO_3$ increases the catalytic activity of the Au_{101}NC-$AlSrTiO_3$:rGO about 64 times with no change in electronic structure and optical properties of the $AlSrTiO_3$. This is attributed to the small particles size and high loading of Au_{101}NC co-catalysts enabled by addition of rGO to the composite. In addition, the selective loading of Au onto rGO over $AlSrTiO_3$ improves

electron–hole separation and facilitates fast charge transfer to the active site and promotes photocatalytic H_2 production. This methodology provides a simple and new avenue to design photocatalysts using graphene-PPh_3-ligated AuNCs as effective co-catalysts for photocatalytic reactions.

Supplementary Materials: The following supporting information can be downloaded at: https://www.mdpi.com/article/10.3390/nano12203638/s1, Figure S1. The SEM image of $AlSrTiO_3$; Figure S2. (a,b) HAADF-STEM images and (c) size distribution histogram of unsupported Au_{101}NC drop-cast onto a TEM grid from methanol solution; Figure S3. BF-STEM images of Au_{101}NC-$AlSrTiO_3$:rGO (a) before and (b) after HER and Au_{101}NC-rGO:$AlSrTiO_3$ (c) before and (d) after HER. Au mass loading: 0.05 wt%. Annealing was performed at 210 °C in air for 15 min; Figure S4. EDX spectra of a chosen spot on (a) rGO in Au_{101}NC-$AlSrTiO_3$:rGO and (b) $AlSrTiO_3$ in Au_{101}NC-rGO:$AlSrTiO_3$. Annealing was performed at 210 °C in air for 15 min. The inserts are the HAADF-STEM images of the chosen area; Figure S5. EDX spectra of a chosen spot on rGO in (a) Au_{101}NC-$AlSrTiO_3$:rGO-HER and (b) Au_{101}NC-rGO:$AlSrTiO_3$-HER. Annealing was performed at 210 °C in air for 15 min. The inserts are the HAADF-STEM images of the chosen area; Figure S6. UV Vis DRS of Au_{101}NC-$AlSrTiO_3$:rGO and Au_{101}NC-rGO:$AlSrTiO_3$ compared to $AlSrTiO_3$ (a) before and (b) after HER. Annealing was performed in air at 210 °C for 15 min; Figure S7. Sacrificial liquid-phase H_2 photocatalysis of Au_{101}NC-$AlSrTiO_3$:rGO (210 °C in air for 15 min) with Au mass loading of 0.05 and 1 wt%. (Conditions: 1:2 methanol:water, 365 nm at 83 mW/cm^2, 2 h reaction time); Figure S8. Sacrificial liquid-phase H_2 photocatalysis of unannealed, annealed (air), and annealed (vacuum) Au_{101}NC-$AlSrTiO_3$:rGO. Au mass loading 1 wt%, 1:2 methanol:water, LED 365 nm at 83 mW/cm^2 for 2 h. Annealing was performed at 210 °C for 15 min; Figure S9. Photographs showing sample dispersions of (a) Au_{101}NC-$AlSrTiO_3$:rGO and (b) Au_{101}NC-rGO:$AlSrTiO_3$ before (left images) and after (right images) photocatalytic HER. Au mass loading 0.05 wt%, 1:2 methanol:water, LED 365 nm at 83 mW/cm^2 for 2 h. Annealing was performed at 210 °C in air for 15 min; Figure S10. Photographs showing dispersions of Au_{101}NCs (1 mg mL^{-1}) in (a) 1:2 methanol:water and (b) methanol. Table S1. Average external quantum efficiencies (EQE)% for synthesized photocatalysts, assuming 2 electrons per H_2 molecule produced. References [28,31] were cited in the Supplementary Materials.

Author Contributions: H.M.: Investigation, validation, methodology, visualization, project administration and designed the experiments, provision of study materials/instrumentation, nanomaterial synthesis, writing—original draft preparation, and leading the manuscript writing; T.D.S.: Photocatalysis measurements/DRS and subsequent analysis, writing the relevant experimental text; S.K.S.: Synthesis of Au_{101}NC and manuscript editing; V.B.G.: supervised the synthesis of Au_{101}NC and manuscript editing; C.J.S.: SEM characterisation, supervision, advisory support, and manuscript review and editing; G.F.M.: funding acquisition, supervision, manuscript review and editing, and final approval of the paper for publication. All authors have read and agreed to the published version of the manuscript.

Funding: This research was funded by the Australian Solar Thermal Research Initiative (ASTRI) program, which, is supported by the Australian Government, through the Australian Renewable Energy Agency (ARENA). H.M. wishes to acknowledge the University of Adelaide for the awarding of a postgraduate scholarship. SKS acknowledges funding support of the UC Connect PhD scholarship. CJS acknowledges funding support from The Australian Research Council (ARC) for a Future Fellowship (FT190100854).

Data Availability Statement: The majority of data created during this study are available within this manuscript and its Supplemental Material. All other data is available upon reasonable request to the corresponding author.

Acknowledgments: H.M would like to acknowledge Domen Kazunari from the University of Tokyo for providing the $AlSrTiO_3$ sample. The authors acknowledge the instruments and scientific and technical assistance of Microscopy Australia at Adelaide Microscopy, The University of Adelaide, a facility that is funded by the University, and State and Federal Governments.

Conflicts of Interest: The authors declare no conflict of interest.

References

1. IEA. *Net Zero by 2050*; International Energy Agency: Paris, France, 2021. Available online: https://www.iea.org/reports/net-zero-by-2050 (accessed on 8 February 2022).
2. Taibi, E.; Miranda, R.; Vanhoudt, W.; Winkel, T.; Lanoix, J.-C.; Barth, F. *Hydrogen from Renewable Power: Technology Outlook for the Energy Transition*; International Renewable Energy Agency: Abu Dhabi, United Arab Emirates, 2018.
3. Pareek, A.; Dom, R.; Gupta, J.; Chandran, J.; Adepu, V.; Borse, P.H. Insights into renewable hydrogen energy: Recent advances and prospects. *Mater. Sci. Energy Technol.* **2020**, *3*, 319–327. [CrossRef]
4. Chen, Y.; Wang, Y.; Li, W.; Yang, Q.; Hou, Q.; Wei, L.; Liu, L.; Huang, F.; Ju, M. Enhancement of photocatalytic performance with the use of noble-metal-decorated TiO_2 nanocrystals as highly active catalysts for aerobic oxidation under visible-light irradiation. *Appl. Catal. B* **2017**, *210*, 352–367. [CrossRef]
5. Wang, Y.; Chen, Y.; Hou, Q.; Ju, M.; Li, W. Coupling plasmonic and cocatalyst nanoparticles on n–TiO_2 for visible-light-driven catalytic organic synthesis. *Nanomaterials* **2019**, *9*, 391. [CrossRef] [PubMed]
6. Li, X.; Wang, W.; Dong, F.; Zhang, Z.; Han, L.; Luo, X.; Huang, J.; Feng, Z.; Chen, Z.; Jia, G.; et al. Recent advances in noncontact external-field-assisted photocatalysis: From fundamentals to applications. *ACS Catal.* **2021**, *11*, 4739–4769. [CrossRef]
7. Yang, J.; Wang, D.; Han, H.; Li, C. Roles of cocatalysts in photocatalysis and photoelectrocatalysis. *Acc. Chem. Res.* **2013**, *46*, 1900–1909. [CrossRef] [PubMed]
8. Chiang, T.H.; Lyu, H.; Hisatomi, T.; Goto, Y.; Takata, T.; Katayama, M.; Minegishi, T.; Domen, K. Efficient photocatalytic water splitting using Al-doped $SrTiO_3$ coloaded with molybdenum oxide and rhodium–chromium oxide. *ACS Catal.* **2018**, *8*, 2782–2788. [CrossRef]
9. Patial, S.; Hasija, V.; Raizada, P.; Singh, P.; Khan Singh, A.A.P.; Asiri, A.M. Tunable photocatalytic activity of $SrTiO_3$ for water splitting: Strategies and future scenario. *J. Environ. Chem. Eng.* **2020**, *8*, 103791. [CrossRef]
10. Ham, Y.; Hisatomi, T.; Goto, Y.; Moriya, Y.; Sakata, Y.; Yamakata, A.; Kubota, J.; Domen, K. Flux-mediated doping of $SrTiO_3$ photocatalysts for efficient overall water splitting. *J. Mater. Chem. A* **2016**, *4*, 3027–3033. [CrossRef]
11. Goto, Y.; Hisatomi, T.; Wang, Q.; Higashi, T.; Ishikiriyama, K.; Maeda, T.; Sakata, Y.; Okunaka, S.; Tokudome, H.; Katayama, M.; et al. A particulate photocatalyst water-splitting panel for large-scale solar hydrogen generation. *Joule* **2018**, *2*, 509–520. [CrossRef]
12. Takata, T.; Jiang, J.; Sakata, Y.; Nakabayashi, M.; Shibata, N.; Nandal, V.; Seki, K.; Hisatomi, T.; Domen, K. Photocatalytic water splitting with a quantum efficiency of almost unity. *Nature* **2020**, *581*, 411–414. [CrossRef]
13. Munir, A.; Joya, K.S.; Ul Haq, T.; Babar, N.-U.-A.; Hussain, S.Z.; Qurashi, A.; Ullah, N.; Hussain, I. Metal nanoclusters: New paradigm in catalysis for water splitting, solar and chemical energy conversion. *ChemSusChem* **2019**, *12*, 1517–1548. [CrossRef]
14. Attia, Y.; Samer, M. Metal clusters: New era of hydrogen production. *Renew. Sustain. Energy Rev.* **2017**, *79*, 878–892. [CrossRef]
15. Yu, C.; Li, G.; Kumar, S.; Kawasaki, H.; Jin, R. Stable Au_{25} (Sr) $_{18}$/TiO_2 composite nanostructure with enhanced visible light photocatalytic activity. *J. Phys. Chem. Lett.* **2013**, *4*, 2847–2852. [CrossRef]
16. Chen, H.; Liu, C.; Wang, M.; Zhang, C.; Luo, N.; Wang, Y.; Abroshan, H.; Li, G.; Wang, F. Visible light gold nanocluster photocatalyst: Selective aerobic oxidation of amines to imines. *ACS Catal.* **2017**, *7*, 3632–3638. [CrossRef]
17. Negishi, Y.; Mizuno, M.; Hirayama, M.; Omatoi, M.; Takayama, T.; Iwase, A.; Kudo, A. Enhanced photocatalytic water splitting by $BaLa_4Ti_4O_{15}$ loaded with ~1 nm gold nanoclusters using glutathione-protected Au_{25} clusters. *Nanoscale* **2013**, *5*, 7188–7192. [CrossRef]
18. Stamplecoskie, K.G.; Kamat, P.V. Size-dependent excited state behavior of glutathione-capped gold clusters and their light-harvesting capacity. *J. Am. Chem. Soc.* **2014**, *136*, 11093–11099. [CrossRef] [PubMed]
19. Madridejos, J.M.L.; Harada, T.; Falcinella, A.J.; Small, T.D.; Golovko, V.B.; Andersson, G.G.; Metha, G.F.; Kee, T.W. Optical properties of the atomically precise C_4 core $[Au_9(PPh_3)_8]^{3+}$ cluster probed by transient absorption spectroscopy and time-dependent density functional theory. *J. Phys. Chem. C* **2021**, *125*, 2033–2044. [CrossRef]
20. Liu, S.; Xu, Y.-J. Photo-induced transformation process at gold clusters-semiconductor interface: Implications for the complexity of gold clusters-based photocatalysis. *Sci. Rep.* **2016**, *6*, 22742. [CrossRef]
21. Puangpetch, T.; Chavadej, S.; Sreethawong, T. Hydrogen production over Au-loaded mesoporous-assembled $SrTiO_3$ nanocrystal photocatalyst: Effects of molecular structure and chemical properties of hole scavengers. *Energy Convers. Manag.* **2011**, *52*, 2256–2261. [CrossRef]
22. Liu, L.; Corma, A. Metal catalysts for heterogeneous catalysis: From single atoms to nanoclusters and nanoparticles. *Chem. Rev.* **2018**, *118*, 4981–5079. [CrossRef]
23. Adnan, R.H.; Madridejos, J.M.L.; Alotabi, A.S.; Metha, G.F.; Andersson, G.G. A review of state of the art in phosphine ligated gold clusters and application in catalysis. *Adv. Sci.* **2022**, *9*, 2105692. [CrossRef] [PubMed]
24. Chen, H.; Peng, L.; Bian, Y.; Shen, X.; Li, J.; Yao, H.-C.; Zang, S.-Q.; Li, Z. Exerting charge transfer to stabilize Au nanoclusters for enhanced photocatalytic performance toward selective oxidation of amines. *Appl. Catal. B* **2021**, *284*, 119704. [CrossRef]
25. Qin, Z.; Zhao, D.; Zhao, L.; Xiao, Q.; Wu, T.; Zhang, J.; Wan, C.; Li, G. Tailoring the stability, photocatalysis and photoluminescence properties of Au_{11} nanoclusters via doping engineering. *Nanoscale Adv.* **2019**, *1*, 2529–2536. [CrossRef] [PubMed]
26. Qin, Z.; Hu, S.; Han, W.; Li, Z.; Xu, W.W.; Zhang, J.; Li, G. Tailoring optical and photocatalytic properties by single-Ag-atom exchange in $Au_{13}Ag_{12}(PPh_3)_{10}Cl_8$ nanoclusters. *Nano Res.* **2022**, *15*, 2971–2976. [CrossRef]

27. Longo, A.; de Boed, E.J.J.; Mammen, N.; van der Linden, M.; Honkala, K.; Häkkinen, H.; de Jongh, P.E.; Donoeva, B. Towards atomically precise supported catalysts from monolayer-protected clusters: The critical role of the support. *Chem. Eur. J.* **2020**, *26*, 7051–7058. [CrossRef] [PubMed]
28. Mousavi, H.; Yin, Y.; Howard-Fabretto, L.; Sharma, S.K.; Golovko, V.; Andersson, G.G.; Shearer, C.J.; Metha, G.F. Au_{101}–rGO nanocomposite: Immobilization of phosphine-protected gold nanoclusters on reduced graphene oxide without aggregation. *Nanoscale Adv.* **2021**, *3*, 1422–1430. [CrossRef]
29. Hu, M.; Yao, Z.; Wang, X. Graphene-based nanomaterials for catalysis. *Ind. Eng. Chem. Res.* **2017**, *56*, 3477–3502. [CrossRef]
30. Shearer, C.J.; Eder, D. 5. Synthesis strategies of nanocarbon hybrids. In *Nanocarbon-Inorganic Hybrids: Next Generation Composites for Sustainable Energy Applications*; Dominik, E., Robert, S., Eds.; De Gruyter: Berlin, Germany, 2014; pp. 125–170.
31. Albero, J.; Mateo, D.; García, H. Graphene-based materials as efficient photocatalysts for water splitting. *Molecules* **2019**, *24*, 906. [CrossRef]
32. Anderson, D.P.; Alvino, J.F.; Gentleman, A.; Qahtani, H.A.; Thomsen, L.; Polson, M.I.J.; Metha, G.F.; Golovko, V.B.; Andersson, G.G. Chemically-synthesised, atomically-precise gold clusters deposited and activated on titania. *Phys. Chem. Chem. Phys.* **2013**, *15*, 3917–3929. [CrossRef]
33. Ruzicka, J.-Y.; Abu Bakar, F.; Hoeck, C.; Adnan, R.; McNicoll, C.; Kemmitt, T.; Cowie, B.C.; Metha, G.F.; Andersson, G.G.; Golovko, V.B. Toward control of gold cluster aggregation on TiO_2 via surface treatments. *J. Phys. Chem. C* **2015**, *119*, 24465–24474. [CrossRef]
34. Wang, C.; Li, N.; Wang, Q.; Tang, Z. Hybrid nanomaterials based on graphene and gold nanoclusters for efficient electrocatalytic reduction of oxygen. *Nanoscale Res. Lett.* **2016**, *11*, 336. [CrossRef]
35. Weare, W.W.; Reed, S.M.; Warner, M.G.; Hutchison, J.E. Improved synthesis of small (dcore $\approx$ 1.5 nm) phosphine-stabilized gold nanoparticles. *J. Am. Chem. Soc.* **2000**, *122*, 12890–12891. [CrossRef]
36. Wang, Q.; Domen, K. Particulate photocatalysts for light-driven water splitting: Mechanisms, challenges, and design strategies. *Chem. Rev.* **2020**, *120*, 919–985. [CrossRef]
37. Mondal, A.; Prabhakaran, A.; Gupta, S.; Subramanian, V.R. Boosting photocatalytic activity using reduced graphene oxide (rGO)/semiconductor nanocomposites: Issues and future scope. *ACS Omega* **2021**, *6*, 8734–8743. [CrossRef]
38. Mousavi, H.; Yin, Y.; Sharma, S.K.; Gibson, C.T.; Golovko, V.; Andersson, G.G.; Shearer, C.J.; Metha, G.F. Factors influencing catalytic activity of size-specific triphenylphosphine-ligated gold nanoclusters in the electrocatalytic hydrogen evolution reaction. *J. Phys. Chem. C* **2022**, *126*, 246–260. [CrossRef]
39. Kurashige, W.; Kumazawa, R.; Mori, Y.; Negishi, Y. Au_{25} cluster-loaded $SrTiO_3$ water-splitting photocatalyst; preparation and elucidation of the effect of cocatalyst refinement on photocatalytic activity. *J. Mater. Appl.* **2018**, *7*, 1–11.
40. Kurashige, W.; Kumazawa, R.; Ishii, D.; Hayashi, R.; Niihori, Y.; Hossain, S.; Nair, L.V.; Takayama, T.; Iwase, A.; Yamazoe, S.; et al. Au_{25}-loaded $BaLa_4Ti_4O_{15}$ water-splitting photocatalyst with enhanced activity and durability produced using new chromium oxide shell formation method. *J. Phys. Chem. C* **2018**, *122*, 13669–13681. [CrossRef]
41. Luo, J.; Li, D.; Yang, Y.; Liu, H.; Chen, J.; Wang, H. Preparation of Au/reduced graphene oxide/hydrogenated TiO_2 nanotube arrays ternary composites for visible-light-driven photoelectrochemical water splitting. *J. Alloys Compd.* **2016**, *661*, 380–388. [CrossRef]
42. Bharad, P.A.; Sivaranjani, K.; Gopinath, C.S. A rational approach towards enhancing solar water splitting: A case study of Au–rGO/n-rGO–TiO_2. *Nanoscale* **2015**, *7*, 11206–11215. [CrossRef] [PubMed]
43. Si, J.; Yu, L.; Wang, Y.; Huang, Z.; Homewood, K.; Gao, Y. Colour centre controlled formation of stable sub-nanometer transition metal clusters on TiO_2 nanosheet for high efficient H_2 production. *Appl. Surf. Sci.* **2020**, *511*, 145577. [CrossRef]
44. Schweinberger, F.F.; Berr, M.J.; Döblinger, M.; Wolff, C.; Sanwald, K.E.; Crampton, A.S.; Ridge, C.J.; Jäckel, F.; Feldmann, J.; Tschurl, M.; et al. Cluster size effects in the photocatalytic hydrogen evolution reaction. *J. Am. Chem. Soc.* **2013**, *135*, 13262–13265. [CrossRef] [PubMed]